Enhanced spin current transmissivity in Pt/$CoFe_2O_4$ bilayers with thermally induced interfacial magnetic modification

M. Gamino,[1,2,*] A. B. Oliveira,[1] D. S. Maior,[3] P. R. T. Ribeiro,[3,4] F. L. A. Machado,[3] T. J. A. Mori,[5] M. A. Correa,[1] F. Bohn,[1] R. L. Rodríguez-Suárez,[6,7] J. Fontcuberta,[2] and S. M. Rezende[3]

[1]*Departamento de Física, Universidade Federal do Rio Grande do Norte, 59078-900 Natal, RN, Brazil*
[2]*Institut de Ciència de Materials de Barcelona (ICMAB-CSIC), Campus UAB, 08193 Bellaterra, Catalonia, Spain*
[3]*Departamento de Física, Universidade Federal de Pernambuco, 50670-901 Recife, Pernambuco, Brazil*
[4]*Instituto de Física Gleb Wataghin, Universidade Estadual de Campinas, Unicamp 13083-859, Campinas, SP, Brazil*
[5]*Laboratório Nacional de Luz Síncrotron, Centro Nacional de Pesquisa em Energia e Materiais, 13083-970, Campinas, SP, Brazil*
[6]*Facultad de Física, Pontifícia Universidad Católica de Chile, Casilla 306, Santiago, Chile*
[7]*Centro de Investigácion em Nanotecnologia y Materiales Avanzados CIEN-UC, Pontifica Universidad Católica de Chile, Av. Vicuña Mackenna 4860, Casilla 306, Santiago, Chile*

(Received 28 March 2023; revised 1 November 2023; accepted 3 November 2023; published 1 December 2023)

We report on processes of generation of spin current and conversion into charge current in $CoFe_2O_4$/Pt bilayers by means of spin Hall magnetoresistance (SMR) and spin Seebeck effect (SSE) experiments. Specifically, we explore (001) full-textured $CoFe_2O_4$ (CFO) thin films grown onto (001)-oriented $SrTiO_3$ substrates, covered with Pt layers deposited under two different conditions: one at room temperature and another at high temperature (400 °C). The x-ray absorption spectroscopy measurements indicate that the Pt layer deposited at high temperature induces an interfacial magneticlike phase (Fe,Co)-Pt alloy, which influences the magnetic behavior of the structure and is responsible for the enhancement of the spin transmission at the interface. By analyzing the SMR data, we conclude that collinear and noncollinear magnetic domains coexist at the CFO-(Fe,Co)-Pt interface. By combining the data from the SMR and SSE measurements, we obtain the ratios between the values of the spin Hall angle (θ_{SH}) and between the ones of the spin-mixing conductance ($g_{eff}^{\uparrow\downarrow}$) in the two samples. We demonstrate that while the value of θ_{SH} decreases by one-half with the heat treatment, the value of $g_{eff}^{\uparrow\downarrow}$ increases by more than one order of magnitude. We interpret the increase of $g_{eff}^{\uparrow\downarrow}$ in terms of unexpected magnetic reconstructions, which produce an enhancement of the magnetic moment arisen at the interface. Since the spin-mixing conductance determines the efficiency of the spin current transmission through the interface, the spinel ferrite cobalt in contact with a normal metal with a suitable heat treatment becomes a promising material for spintronics device applications.

DOI: 10.1103/PhysRevB.108.224402

I. INTRODUCTION

One of the main goals of research in the field of spintronics resides in the development of methods for the generation and manipulation of spin currents [1]. Usually, one makes use of a ferromagnetic insulating (FMI) layer having tunable features to change the magnetic and electrical properties of an adjacent nonmagnetic (NM) metallic layer with strong spin-orbit coupling. It is well known that the properties of the NM can be modified when the FMI is brought close enough in the FMI/NM interfaces; such phenomenon is known as the magnetic proximity effect [2–4]. This effect can manifest through the induction of a magnetization in paramagnetic materials due to short-range proximity, which is of the order of a few nanometers for materials that are close to satisfying the Stoner criterion for ferromagnetism, such as Pt and Pd. Understanding the features of the interface between FMI and NM layers, and how the surface magnetism and spin transport interact with each other, is a key for clarifying the dominant mechanisms in the spin-to-charge currents interconversion process in several spintronic phenomena. Among these phenomena, we may highlight the spin Hall effect (SHE) [5,6], Rashba-Edelstein effect [7–12], inverse spin Hall effect (ISHE) [12–17], and spin Hall magnetoresistance (SMR) [18,19]. The SMR originates from a combination of spin Hall and inverse spin Hall effects in the NM layer, due to reflected spin currents at the FMI/NM interface and it is generally associated with the relative orientation between the spin current polarization in the NM layer and the magnetization direction of the ferromagnetic layer [18–21].

Generally, most studies with SMR have focused on FMI/NM heterostructures with collinear magnetic configurations. It is quite interesting that only a few SMR investigations have explored the noncollinear and/or canted magnetic configurations of the FMI magnetization layer [22–26], given that they offer an excellent playground for the scrutiny of interactions between surface magnetic ordering and spin transport phenomena. In the last several years, spinel insulating oxides, such as cobalt ferrite ($CoFe_2O_4$; CFO) [27–32],

*Corresponding author: mgamino@fisica.ufrn.br

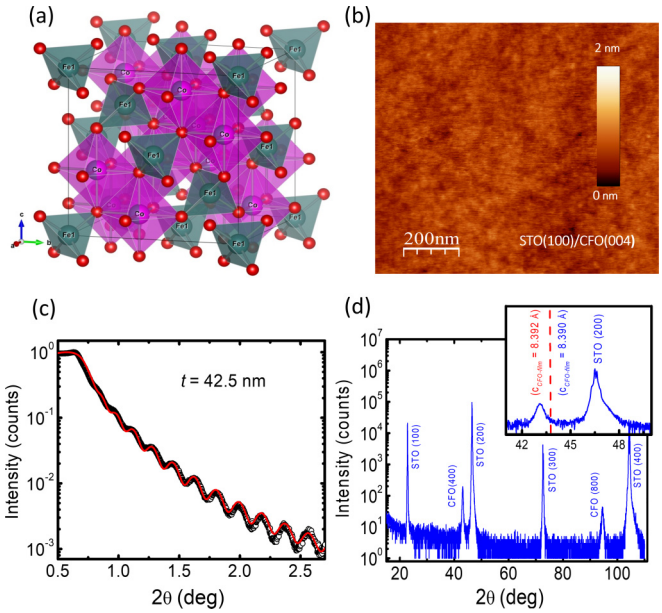

FIG. 1. (a) Cubic inverse spinel structure of CFO with the Co^{2+} cations located in the octahedral sites (purple) and Fe^{3+} cations equally distributed in the tetrahedral (green) and the octahedral sites. The oxygen ions are identified by red circles. (b) Atomic force microscopy image ($1 \times 1\,\mu m^2$) of the STO/CFO sample. (c) X-ray reflectivity spectra of the CFO thin film. The solid red line across the XRR data indicates best fitting for the thickness calibration. (d) The ($\theta-2\theta$) x-ray diffraction pattern obtained for the STO/CFO sample.

have shown up as promising candidates for spin current injectors, since they own predicates that allow the analysis of the influence of the surface magnetic configuration on the spin transport in FMI/NM heterostructures. CFO particularly has a cubic inverse spinel structure, as illustrated in Fig. 1(a), where the Co^{2+} cations are in octahedral sites and the Fe^{3+} ones are equally distributed in the tetrahedral and octahedral sites. The ferrimagnetic order of CFO is determined by the strong exchange interaction (antiferromagnetic) between the magnetic moments of the tetrahedral (Fe^{3+}) and octahedral (Co^{2+}) sites, which couple through an overlap of the $3d$ orbitals with the $2p$ orbitals of the intermediate oxygen anion. As the Fe^{3+} cations of the tetrahedral and octahedral sites cancel out due to antiferromagnetic coupling, the saturation magnetization of the CFO is close to that of the cobalt (magnetization of 376 emu/cm^3 and magnetic moment of $3\mu_B$). However, engineered CFO thin films bring together interesting, yet puzzling magnetic properties that differ from those found in bulk, such as the enhanced magnetization and large magnetic anisotropy (i.e., magnetocrystalline and magnetoelastic properties) induced by the epitaxial strain that can be handled by a suitable choice of the substrate [33–35]. In addition, CFO thin films present relevant surface magnetic anisotropy. In particular, CFO thin films are commonly characterized by presenting antiphase boundaries (APBs) [36–39], which are structural defects breaking the crystalline order. In this sense, the degree of epitaxy associated to the substrate affects the APBs density. Hence, surface magnetic anisotropy effects, as well as complex magnetic interactions lead to strong changes of the magnetic properties with respect to those found for the bulk material. Therefore, CFO thin films present some peculiar magnetic properties that may undergo electronic and/or atomic changes at the CFO-Pt interface.

In this paper, we report an investigation of CFO/Pt bilayers with (001) full-textured CFO thin films grown onto (001)-oriented $SrTiO_3$ substrates using spin-to-charge interconversion processes measured by means of spin Hall magnetoresistance and spin Seebeck effect (SSE). The motivation is based on the results reported in Ref. [30] showing that the deposition of the Pt layer under different temperatures produces quite different structural, electronic, and magnetic properties. To clarify the structures and mechanisms involved we prepare CFO/Pt bilayers with the Pt layers grown under two different conditions: one at room temperature (sample CFO/Pt@RT) and the other at a high temperature of 400 °C (sample CFO/Pt@HT). X-ray absorption spectroscopy (XAS) measurements indicate that the Pt layer deposited at a high temperature induces a new interfacial magnetic phase like (Fe, Co)-Pt alloy, which influences the magnetic behavior of the structure and is responsible for the enhancement of the spin transmission at the interface. The angular-dependent magnetoresistance (ADMR) results are interpreted using a model that takes into account collinear and noncollinear magnetic domains at the CFO-(Fe,Co)-Pt interface. By combining SMR and SSE measurements, we obtain a value for the spin Hall angle (θ_{SH}) for the CFO/Pt@RT that is larger than the one estimated for the CFO/Pt@HT sample; the spin-mixing conductance ($g_{eff}^{\uparrow\downarrow}$) in turn displays the opposite trend, increasing by more than one order of magnitude when Pt is deposited at high temperature. We explain the increase of $g_{eff}^{\uparrow\downarrow}$ in terms of unexpected magnetic reconstructions, which lead to an enhancement of the magnetic moment arisen at the interface. Thus, we show that the SMR is a highly sensitive probe to surface magnetism that can be used to identify even complex magnetic configurations, including collinear and noncollinear magnetic domains at FMI/NM interfaces. We also observe a strong dependence of the SSE current with the Pt layer deposition temperature, which is fully consistent with the SMR results.

The paper is organized as follows: In Sec. II, we describe the sample preparation and structure characterization by x-ray reflectivity, x-ray diffraction, and atomic force microscopy (AFM). In Sec. III, we show x-ray absorption spectroscopy results using two detection modes used concurrently: total electron yield and fluorescence yield. In Sec. IV, we show and discuss the magnetization measurements. In Sec. V, we discuss the field-dependent magnetoresistance measurements. In Sec. VI, we present the experimental results and theoretical considerations of the ADMR measurements. In Sec. VII, we address the spin Seebeck measurements. Finally, in Sec. VIII, we compare the results of the two techniques and obtain the ratios between the values for the spin Hall angle (θ_{SH}) and the spin-mixing conductance ($g_{eff}^{\uparrow\downarrow}$) for the two samples.

II. SAMPLE PREPARATION AND STRUCTURAL CHARACTERIZATION

CFO thin films with thickness of 42 nm are grown onto (001)-oriented $SrTiO_3$ (STO) substrates with lateral dimensions $5 \times 5\,mm^2$. The films are prepared from a CFO

stoichiometric target by pulsed laser deposition using a KrF laser ($\lambda = 248$ nm) with fluence of 1.5 J/cm^2 and a repetition rate of 5 Hz at 450 °C in an oxygen pressure of 0.1 mbar. The typical surface roughness of the films grown under these conditions is ∼0.13 nm (1 μm × 1 μm area scans). The CFO films, grown in the same run, are further capped with a dc-sputtered Pt layer either grown *in situ* at room temperature (sample CFO/Pt@RT) or at a high temperature of (400 °C) (sample CFO/Pt@HT). The thicknesses of the CFO films ($t_{CFO} \approx 42$ nm) and Pt layers ($t_{Pt} = 4$ nm) are inferred from the growth rate calibration obtained by x-ray reflectometry (XRR). The θ-2θ x-ray diffraction (XRD) scans confirm that the CFO films are fully (00l) textured without any trace of spurious phases.

Figure 1(b) shows a representative AFM ($1 \times 1\ \mu m^2$) image of the CFO thin film grown onto the STO substrate. The film exhibits a very flat surface with surface roughness estimated to be of 0.13 nm, i.e., less than 1% of its thickness. Figure 1(c) shows the x-ray reflectivity data for the CFO film. The red solid lines are the best fits obtained using Philips WINGIXA software. The well-defined Kiessig fringes confirm that the surface and interface of the thin film are extremely flat. From the XRR fit, the values of the density, surface roughness, and thickness of CFO thin films are found to be ≈ 5.12 g/cm^3, 0.17 nm (rms), and 42.5 nm, respectively. The obtained density and the roughness values are in excellent agreement with the theoretical value (5.3 g/cm^3) and the AFM value (0.13 nm), respectively. The CFO films grown on STO substrates consistently have *c*-axis texture with the [100] CFO parallel to the [100] STO. The x-ray diffraction patterns in Fig. 1(d) show that the CFO film is fully (00l) oriented without traces of any spurious phase. The XRD reflections show no shift for smaller or higher angles when comparing to the CFO bulk reflections ($c_{bulk} = 8.392$ Å), indicating that the film has a relaxed out-of-plane lattice parameter (*c* axis), estimated to be of $c_{film} = 8.385$ Å for the (004) plane, as shown in the inset of Fig. 1(d). This structural relaxation can be interpreted in terms of the large mismatch ($\approx 7.4\%$) between the cell parameters of the STO and those of the CFO. This mismatch value is obtained considering two STO unit cells and bulk cell parameters of STO and CFO as $a_{STO} = 3.905$ Å and $a_{CFO} = 8.392$ Å, respectively.

III. X-RAY SPECTROSCOPY

X-ray absorption spectra of samples of the CFO/Pt@RT and CFO/Pt@HT are acquired at the IPE beamline of the Brazilian Synchrotron Light Laboratory (Sirius, LNLS) [40]. The measurements are carried out at room temperature around the L_3 and L_2 absorption edges of both the Fe (700–740 eV) and the Co (770–810 eV) absorbing atoms. The linearly polarized (horizontally) photons reach the sample surface at normal incidence. Here, we use two detection modes concurrently: total electron yield (TEY) and fluorescence yield (FY). Although the fluorescence cross section is much lower in the soft x-ray range (requiring more acquisition statistics), the FY mode provides a reliable method to obtain an x-ray absorption spectrum that is averaged along the full depth of the CFO film, since the photon-in/photon-out signal is bulk sensitive. On the other hand, the TEY signal is surface sensitive, probing just a few nanometers from the CFO/Pt interface (with maximum weight to the interface and decaying exponentially with depth).

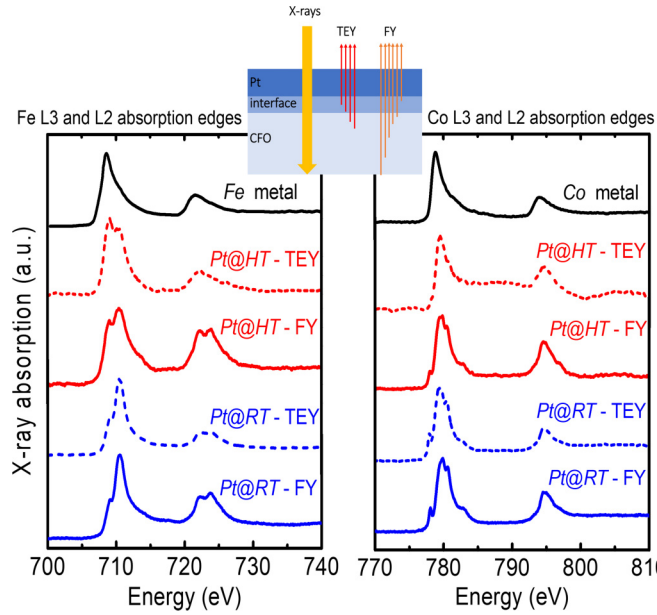

FIG. 2. X-ray absorption spectra around the L_3 and L_2 absorption edges of Fe (left) and Co (right) for samples CFO/Pt@RT (blue) and CFO/Pt@HT (red), in addition to the Fe^0 and Co^0 reference spectra (black) acquired from standard metallic samples. The spectra are measured concurrently by both FY (solid lines) and TEY (dashed lines) modes. The sketch (center) represents the XAS experiment: although the x rays go through the entire film and the FY signal is also averaged from photons generated along the full depth of the CFO, the TEY signal probes only a few nanometers from the CFO/Pt interface (with maximum weight to the interface and decaying exponentially with depth). All spectra are normalized by their maximum intensity for easy comparison of their line shapes.

The x-ray absorption process involves the transition from a core electron to the empty states above the Fermi level, thus probing the electronic structure of the valence levels. Specifically, the *L*-edge absorption spectrum [excitation of the $2p^{1/2}$ (L_2 peak) and $2p^{3/2}$ (L_3 peak) core levels] of transition metals and their oxides is representative of the empty $3d$ valence states. A metal spectrum, such as for Fe^0 and Co^0 (Fig. 2, black), exhibits two broad peaks that reveal the width of the empty valence bands. On the other hand, an oxide spectrum presents a more prominent fine structure, disclosing more localized empty states. The energies of the so-called multiplet structure are mainly determined by crystal field effects.

Figure 2 shows the spectra measured for samples CFO/Pt@RT (blue) and CFO/Pt@HT (red), together with the metal spectra obtained from a standard reference. In the case of sample CFO/Pt@RT, both Fe (left) and Co (right) spectra present fine structures that are very similar to those of the cobalt ferrite spectra reported in the literature [41,42]. While the Fe spectra is very characteristic of a film containing mostly Fe^{3+} cations, the Co spectra is typical of Co^{2+} in octahedral sites [42]. It is important to notice that the similarity between the spectra acquired by TEY (dashed lines) and FY (solid lines) confirms that both Fe and Co ions can be found in

these oxidized states throughout the entire CFO layer. On the other hand, the spectra obtained by the TEY of sample CFO/Pt@HT greatly differ from the one measured by FY. While the FY spectra of both Fe and Co L edges resemble the fine structure observed for sample CFO/Pt@RT as described above, the TEY spectra show a clear trend to more metallic states, i.e., Fe^0 and Co^0. Given that the CFO/Pt interface contributes much more to the TEY signal, these results suggest that a (Fe,Co)-Pt alloy is likely being formed at the sample CFO/Pt@HT's interface, according to the results reported in Ref. [30]. Moreover, the alloying interface arising from the Pt deposition at high temperature strongly affects the magnetic and spin transport properties of the system, as will be discussed in the following sections.

IV. MAGNETIZATION MEASUREMENTS

Before discussing the magnetization results, it is fundamental to recall that CFO thin films, as previously mentioned in Sec. I, exhibit APBs caused by the stacking faults during the growth of the films. This prevents CFO films from reaching their saturation magnetization due to the introduction of antiferromagnetic domains with hard saturation magnetization [36–38] and considerable surface magnetic anisotropy [33], such as the creation of magnetic domains with complex competing interactions that contribute to the reduction of the saturation magnetization. However, distinct features can be observed in CFO films deposited onto different substrates, such as a spinel $MgAl_2O_4$, which presents large magnetic anisotropy and large magnetization at high magnetic fields, due to, for instance, the induced epitaxial strain [34,39]. In addition, in CFO thin films, some partial inversion occurs so that Co^{2+} ions can also be at the tetrahedral sites that also lead to an increase in the saturation magnetization, rather than a decrease.

The magnetization measurements of the CFO thin films are carried out using a superconducting quantum interference device magnetometer (magnetic properties measurement system of Quantum Design). The magnetization curves are obtained after subtracting the STO substrate diamagnetic linear contribution extrapolated from the high-field regime. Figure 3 shows the room-temperature magnetization curves of the STO/CFO/Pt heterostructures, for Pt layer deposited at room temperature (CFO/Pt@RT) and high temperature (CFO/Pt@HT) obtained with the magnetic field applied in the t axis, i.e., $H \parallel [100]$ (in plane) and n axis, i.e., $H \parallel [001]$ (out of plane).

The in-plane magnetization curve for the CFO/Pt@RT sample exhibits a slightly larger coercive field ($H_C = 3.15$ kOe) in comparison to the out-of-plane ($H_C = 0.4$ kOe) one, as shown in Fig. 3(a). In addition, the remanence for the in-plane curve ($M_r/M_s = 0.25$) is larger than that for the out-of-plane experiment ($M_r/M_s = 0.08$). Notice that the magnetization value at high field (M_s) is about 241 emu/cm^3 for both directions. These magnetic features observed for the CFO/Pt@RT sample are very similar to the values of CFO thin film (without Pt layer), shown in the inset of Fig. 3(a), and previously reported in literature [28,29,33]. On the other hand, the magnetization curves for the CFO/Pt@HT sample, for both directions (in and out of plane), exhibit quite different

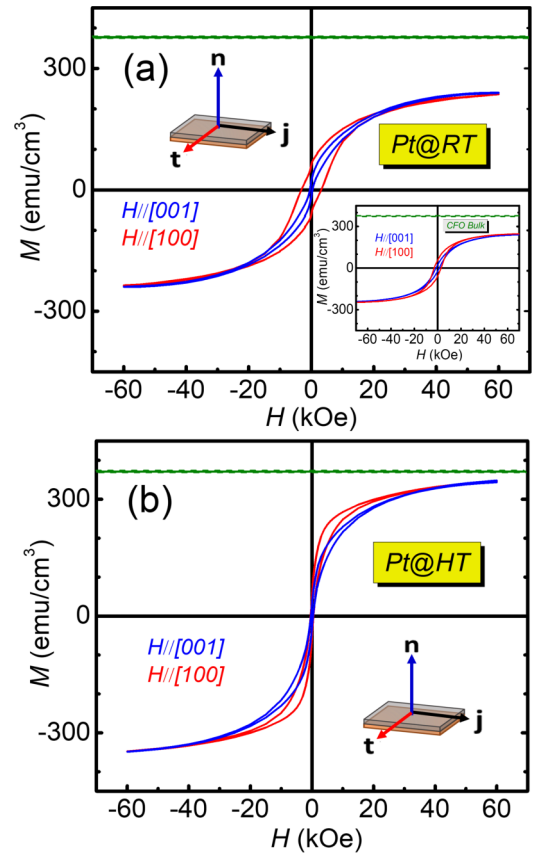

FIG. 3. Magnetization curves for (a) STO/CFO/Pt@RT and (b) STO/CFO/Pt@HT measured at room temperature with $\boldsymbol{H}$ along the $\boldsymbol{t}$ and $\boldsymbol{n}$ directions. The inset shows the magnetization curves for the STO/CFO (42 nm) sample, without the Pt layer, measured at room temperature with $\boldsymbol{H}$ applied along the $\boldsymbol{t}$ and $\boldsymbol{n}$ directions. The dashed green line indicates the magnetization value for CFO bulk ($\sim$376 emu/cm^3).

magnetic behaviors. First, the magnetization value at high magnetic field increases to around 350 emu/cm^3, which is very close to the CFO bulk value, as shown in Fig. 3(b). In addition, in both directions, the coercive field and remanent magnetization display a large decrease to values of $H_C = 0.4$ kOe and $M_r/M_s = 0.07$, respectively.

From these results, one can clearly see an evolution of the magnetization curve of the CFO/Pt@HT sample relative to the CFO/Pt@RT one. This is characterized by the decrease of the magnetic anisotropy evidenced through the reduction of the coercive field, the increase of the magnetization at high fields, and the emergence of a curve with peculiar shape, having a shrink of the curve at low fields, keeping the opening at high magnetization values. It can be understood in terms of the interplay of two processes taking place during the deposition of the Pt layer at the high temperature of 400 ºC. The first process corresponds to slight modifications of the CFO layer. It has been observed previously in literature that post-production heat treatments influence the magnetic and magnetoelastic properties of highly magnetostrictive CFO, promoting a decrease of the anisotropy constant, coercive field, magnetostriction, and strain sensitivity, as well as inducing an increase of the saturation magnetization [43]. It is

worth mentioning that such changes are found even employing temperatures below the one used in the CFO deposition [35]. These changes are not accompanied by any observable changes in crystal structure or composition, but are indicative of the migration of Co^{2+} from the octahedral sites (*B* sites) to the tetrahedral sites (*A* sites) and Fe^{3+} from the *A* sites to the *B* sites of the spinel structure [35,43]. Next, the second process occurring during the Pt deposition at high temperature consists in structural, electronic, and magnetic reconstructions, which gives rise to the formation of the (Fe,Co)-Pt alloy at the CFO/Pt interface [30]. We understand that such alloy contributes to the increase of the magnetization of the structure, as well as being majorly responsible for the peculiar magnetization curve, having both a shrink of the magnetization curve at low fields and the opening at high magnetization levels [33].

V. FIELD-DEPENDENT MAGNETORESISTANCE

The field-dependent magnetoresistance measurements of the CFO/Pt@RT and CFO/Pt@HT samples are carried out at room temperature with an applied magnetic field of up to 90 kOe by using a physical property measurement system (PPMS). Here, the sample plane is defined by the *t* and *j* axes, with the charge current (j_c) flowing along the $\boldsymbol{j}$ direction, the *t* axis as the in-plane transverse direction, and along the out-of-plane direction (*n* axis, perpendicular to both *j* and *t* axes). The magnetoresistance measurements are performed using four inline silver paint strips. The room-temperature longitudinal baseline resistance (R_0) and resistivity (ρ_0) of the Pt layers ($t_{Pt} = 4$ nm) grown at high temperature (HT) 400 °C and room temperature (RT) are ∼201 Ω ($\rho_0 = 38.6\ \mu\Omega$cm) and ∼248 Ω ($\rho_0 = 52.8\ \mu\Omega$cm), respectively.

Figure 4 shows longitudinal magnetoresistance (MR), defined as $\mathrm{MR} = R_L(H) - R_L(0)/R_L(0)$, measured at room temperature in the CFO/Pt@RT and CFO/Pt@HT samples, recorded with ($\boldsymbol{H} \parallel \boldsymbol{j}$), ($\boldsymbol{H} \parallel \boldsymbol{t}$), and ($\boldsymbol{H} \parallel \boldsymbol{n}$). The field-dependent MRs of the CFO/Pt@RT sample decrease with increasing applied field along the *t* direction ($\boldsymbol{H} \parallel \boldsymbol{t}$) and increase for $\boldsymbol{H} \parallel \boldsymbol{j}$ and $\boldsymbol{H} \parallel \boldsymbol{n}$. These MR behaviors for all three directions agree with SMR, which is characterized by $R_L(\boldsymbol{H} \parallel \boldsymbol{n}) \approx R_L(\boldsymbol{H} \parallel \boldsymbol{j}) > R_L(\boldsymbol{H} \parallel \boldsymbol{t})$. On the other hand, for the CFO/Pt@HT sample, the MR decreases with increasing applied magnetic field in all directions, which differs significantly from that in the CFO/Pt@RT sample, as shown in Fig. 4(b). This similar MR behavior has also been observed in Fe_3O_4 thin films and is attributed to the carrier transport across APBs [44–46]. In particular, the non-saturated MR behavior observed for both samples can be related to the Lorentz magnetoresistance of the Pt layers [28,29], as well as to the presence of the APBs. These remarkable features for MR measurements in all directions suggest a strong contribution associated to anisotropic magnetoresistance (AMR) that is characterized by $R_L(\boldsymbol{H} \parallel \boldsymbol{j}) > R_L(\boldsymbol{H} \parallel \boldsymbol{t}) \approx R_L(\boldsymbol{H} \parallel \boldsymbol{n})$. Thus, from these measurements, it is quite clear that the MR of the Pt layer is dramatically modified due to the Pt magnetic nature acquired during their growth. Therefore, we attribute these results to two possible scenarios: one is related to a new orientation of the magnetic domains induced by the CFO surface magnetization components when probed for ($\boldsymbol{H} \parallel \boldsymbol{t}$) and ($\boldsymbol{H} \parallel \boldsymbol{j}$); the second is related to the formation of the (Fe,Co)-Pt metallic ferromagnetic alloy at the Pt/CFO interface due to thermally induced atomic modification when the Pt layer is deposited at high temperature on the CFO film [30].

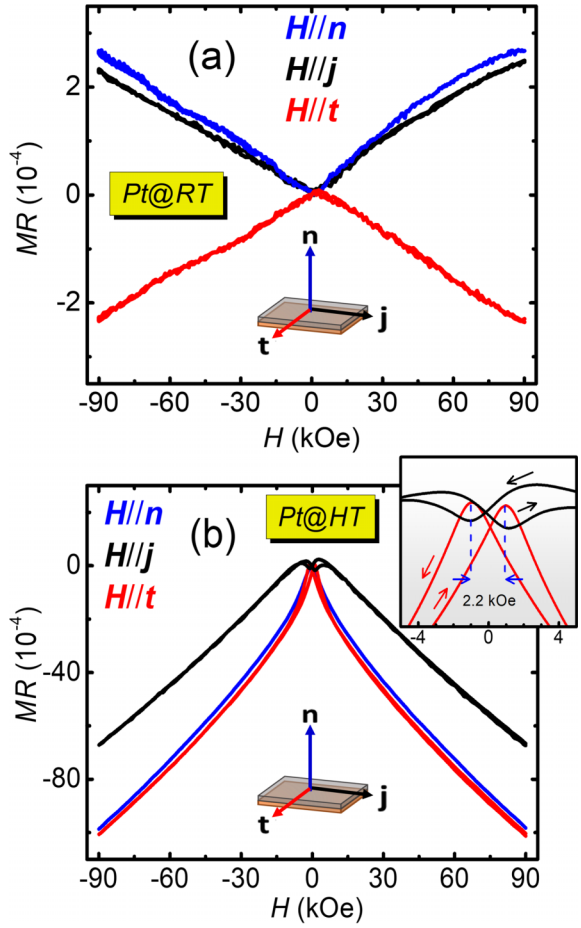

FIG. 4. Longitudinal field-dependent magnetoresistance measured at room temperature with $\boldsymbol{H}$ applied along the $\boldsymbol{t}$, $\boldsymbol{n}$, and $\boldsymbol{j}$ directions for the (a) CFO/Pt@RT and (b) CFO/Pt@HT samples. The inset in Fig. 3(b) displays the MR at low magnetic fields.

Moreover, from a closer look at the MR data in Fig. 4(b), at the low magnetic fields regime (∼+4 kOe to −4 kOe), we observe in-plane hysteresis loops related to the negative MR for $R_L(\boldsymbol{H} \parallel \boldsymbol{t})$ and the positive for $R_L(\boldsymbol{H} \parallel \boldsymbol{j})$. Note that the resistance switching behavior of the $R_L(\boldsymbol{H} \parallel \boldsymbol{j})$ displays two downwards symmetrical peaks: one related to the negative coercive field ($H_c \approx -1.1$ kOe) for the field scan decrease and a second one associated to the positive coercive field ($H_c \approx +1.1$ kOe) for the field scan increase [see the black arrows in the inset of Fig. 4(b)]. The $R_L(\boldsymbol{H} \parallel \boldsymbol{t})$ shows two upwards symmetrical peaks: one related to the field scan decrease and another one to the field scan increase [see the red arrows in the inset of Fig. 4(b)] with coercive fields quite similar to that in $R_L(\boldsymbol{H} \parallel \boldsymbol{j})$. Furthermore, we can notice that the hysteresis observed on $R_L(\boldsymbol{H} \parallel \boldsymbol{j})$ and $R_L(\boldsymbol{H} \parallel \boldsymbol{t})$ exhibits H_c that is different from that found from the magnetization curve of the CFO thin film, as shown in Fig. 4. While for $R_L(\boldsymbol{H} \parallel \boldsymbol{j})$ and $R_L(\boldsymbol{H} \parallel \boldsymbol{t})$ $H_c \approx +1.1$ kOe, for CFO in-plane magnetization, $H_C = 3.05$ kOe. Therefore, we can infer that

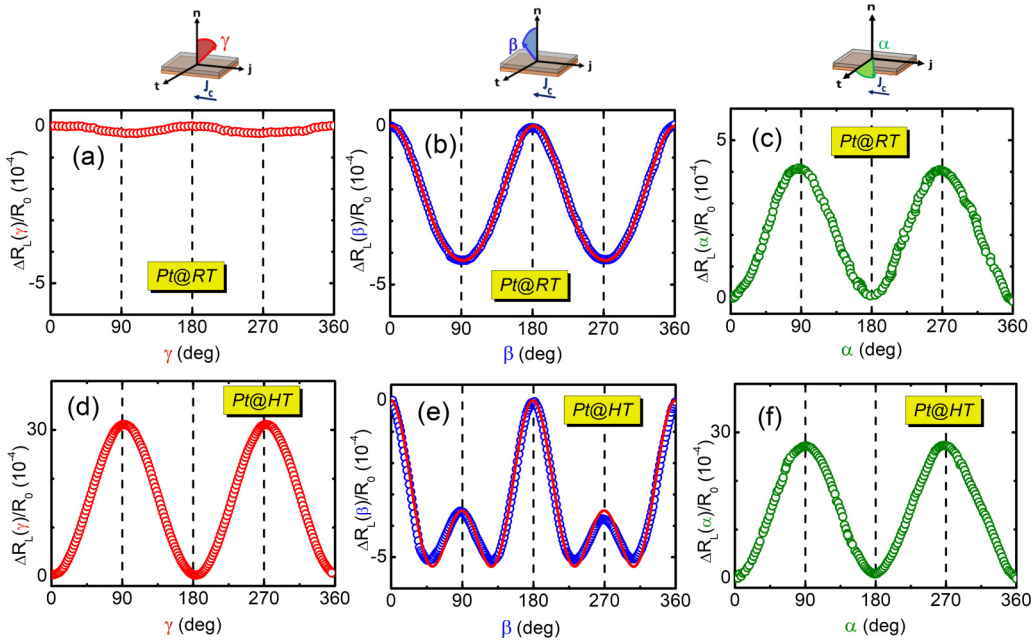

FIG. 5. Longitudinal angle-dependent magnetoresistance measured for a fixed external magnetic field $\boldsymbol{H}$ of 90 kOe. (a) $R_L(\gamma)$, (b) $R_L(\beta)$, and (c) $R_L(\alpha)$ scans for CFO/Pt@RT bilayer. (d) $R_L(\gamma)$, (e) $R_L(\beta)$, and (f) $R_L(\alpha)$ scans for CFO/Pt@HT bilayer. The fixed external magnetic field is applied rotating on the and γ, β, and α angles (schematic illustration shown in the top panels) that define the $\boldsymbol{n}$-$\boldsymbol{j}$, $\boldsymbol{n}$-$\boldsymbol{t}$, and $\boldsymbol{t}$-$\boldsymbol{j}$ planes, respectively. The charge current j_C is always applied in the $\boldsymbol{j}$ direction. The solid red lines in (b) and (e) are the best fittings obtained using Eq. (5); the model that considers collinear and noncollinear magnetic domains at the interface.

the CFO/Pt interfacial magnetic configuration is dominated mainly by the magnetic nature acquired by the Pt layer so that only its own reversal can be observed, while any reversal associated, for instance, to CFO surface magnetization, remains fixed. This situation should only change when the applied magnetic field is large enough to overcome the CFO surface magnetization that seems to occur at around 20 kOe.

VI. ANGULAR-DEPENDENT MAGNETORESISTANCE

One of the most relevant MR effects used to obtain information about the spin configuration at FMI/NM interfaces is the spin Hall magnetoresistance. Since its origin relies on the interplay between spin Hall and inverse spin Hall effects, the SMR is a second-order effect in $\theta_{\rm SH}$. A relevant ingredient in the SMR is the spin transport across the FMI/NM interface, which is quantified by the spin-mixing interfacial conductance (G_r). Thus, both $\theta_{\rm SH}$ and G_r determine the magnitude of the SMR. To further investigate the magnetoresistance effect that arises in the CFO/Pt interfaces, we perform ADMR measurements by rotating the sample holder in the $\boldsymbol{n}$-$\boldsymbol{j}$ (γ scan), $\boldsymbol{n}$-$\boldsymbol{t}$ (β scan), and $\boldsymbol{t}$-$\boldsymbol{j}$ (α scan) planes, as sketched in the top panels in Fig. 5. The longitudinal resistances $R_L(\gamma)$, $R_L(\beta)$ and $R_L(\alpha)$ are recorded at a fixed external magnetic field of 90 kOe. From ADMR measurements, the AMR longitudinal resistance predicted is given by [18,47]

$$\rho_{\rm AMR} = \rho_0 + \Delta\rho m_j^2 = \rho_0 + \Delta\rho \sin^2\gamma, \tag{1}$$

where ρ_0 is the baseline resistivity, $\Delta\rho$ is the amplitude of the AMR, and m_j is the director cosine of the magnetization in the charge current direction ($\boldsymbol{j}$ direction). Unlike AMR, the SMR obtained from ADMR in FMIs with collinear magnetic configurations is given by [18,47]

$$\rho_{SMR} = \rho_0\left[1 - \Delta\rho_1/\rho_0\left(1 - m_t^2\right)\right]^{-1}, \tag{2}$$

where m_t is the director cosine of the magnetization in the $\boldsymbol{t}$ direction, and

$$\frac{\Delta\rho_1}{\rho_0} = \theta_{\rm SH}^2\left(\frac{\lambda_{\rm NM}}{d_{\rm NM}}\right)\frac{2\lambda_{\rm NM}\, G_r \tanh^2\frac{d_{\rm NM}}{2\lambda_{HM}}}{\sigma_{\rm NM} + 2\lambda_{\rm NM} G_r \coth\frac{d_{\rm NM}}{\lambda_{\rm NM}}}. \tag{3}$$

Here $\sigma_{\rm NM}$, $\lambda_{\rm NM}$, $d_{\rm NM}$, and $\theta_{\rm SH}$ are the conductivity, spin diffusion length, thickness, and spin Hall angle of the NM (Pt), respectively, and G_r is the real part of the spin-mixing conductance at the CFO/Pt interface. Notice that the SMR does not contribute to the γ scan magnetoresistance signal. For $\Delta\rho_1/\rho_0 \ll 1$, Eq. (2) can be expanded so that $\rho_{SMR} \approx \rho_0 + \Delta\rho_1(1-m_t^2) \approx \Delta\rho_1\cos^2\beta$ [47]. Thus, as discussed below, this expression can lead to underestimated values of G_r. The ADMR results for the CFO/Pt@RT and CFO/Pt@HT samples on the β, γ, and α scans are defined by

$$\frac{\Delta R_L}{R_0} = \frac{R_L(\beta,\gamma,\alpha) - R_L(\beta,\gamma,\ \alpha\ = 0^0)}{R_0}, \tag{4}$$

where R_0 is the baseline resistance. The $R_L(\gamma)$, $R_L(\beta)$, and $R_L(\alpha)$ measurements for the CFO/Pt@RT sample shown in Figs. 5(a), 5(b), and 5(c), exhibit the usual behavior of FMI/NM bilayers and are consistent with the SMR theory given by Eq. (2). On the other hand, the $R_L(\beta)$ for the CFO/Pt@HT provides an unlike behavior as fourfold symmetry, as shown Fig. 5(e). This behavior opens a new scenario on surface magnetization that can be ascribed to noncollinear magnetic domains or a spin-flop transition at the ferrimagnet surface [23,48–50].

To elucidate and unveil the contribution of the new surface magnetization configuration on the $R_L(\beta)$ measurements, we propose a model which approaches distinct configurations of magnetic domains at the interface. In particular, we consider two noninteracting domains at the CFO-Pt interface that are distinguished for having magnetic moments parallel (collinear) or nonparallel (noncollinear) to the applied field, so that those contribute independently to the SMR. Thereby, in this model the SMR is written as

$$\rho_{SMR} = f_{\rm coll}\rho_{SMR}^{\rm coll} + (1 - f_{\rm coll})\rho_{SMR}^{\rm noncoll}, \tag{5}$$

where $f_{\rm coll}$ represents the fraction of collinear magnetic domains, and

$$\rho_{SMR}^{\rm coll} = \rho_0\left[1 - \Delta\rho_1/\rho_0 \cos^2\left(\beta - \beta_0^{\rm coll}\right)\right]^{-1} \tag{6}$$

and

$$\rho_{SMR}^{\rm noncoll} = \rho_0\left[1 - \Delta\rho_1/\rho_0 \sin^2\left(\beta - \beta_0^{\rm noncoll}\right)\right]^{-1} \tag{7}$$

are the contributions to the SMR resistivity from the collinear and noncollinear domains at the respective magnetic domains with respect to the coordinate axes. The relative abundance of these two kinds of magnetic domains defines the SMR response.

This is a simple model for the spin configuration at the CFO/Pt interface, which is undoubtedly more complex than that mimicked here. According to Eq. (6), the SMR response of a collinear domain looks exactly like in ferrimagnetic insulator/normal metal systems. In contrast, for ferrimagnets with noncollinear magnetic domains, the SMR response depends on the orientation of the magnetic domains with applied magnetic field [25,26]. Note that $\sin^2\beta$ angular dependence in Eq. (7) has been reported in heterostructures of NMs in contact with antiferromagnetic materials [51–54].

Figure 5(b) shows the fit of the experimental data using the model described by Eq. (5) considering collinear and noncollinear magnetic domains ($f_{\rm coll} \neq 1$; solid red line). From the best fitting we obtain $\Delta\rho_1/\rho_0 = 0.012$, $f_{\rm coll} = 0.52$, $\beta_0^{\rm coll} = 0.77^\circ$, and $\beta_0^{\rm noncoll} = 0.7^\circ$. Taking into account $d_{\rm NM} = 4$ nm, $\sigma_{\rm NM} = 10^7\ \Omega\ {\rm m}^{-1}$ and $\lambda_{\rm NM} = 2$ nm for the Pt layer, and knowing $\Delta\rho_1/\rho_0$, from Eq. (3) we obtain $[\theta_{\rm SH}^2\, G_r]_{\rm Pt@RT} = 1.1 \times 10^{14}\ \Omega^{-1}\ {\rm m}^{-2}$; and using $g_{\rm eff}^{\uparrow\downarrow} = G_r e^2/h$, we found $[\theta_{\rm SH}^2 g_{\rm eff}^{\uparrow\downarrow}]_{\rm Pt@RT} = 2.7 \times 10^{18}\ {\rm m}^{-2}$, which is in agreement with values reported in literature [21,27]. Now, considering only collinear magnetic domains $f_{\rm coll} = 1$, from the best fitting (not shown) we obtain $\Delta\rho_1/\rho_0 = 0.00045$, $\beta_0^{\rm coll} = 1.5^\circ$, that from Eq. (3) yields $[\theta_{\rm SH}^2\, G_r]_{\rm Pt@RT} = 3.8 \times 10^{12}\ \Omega^{-1}\ {\rm m}^{-2}$ or $[\theta_{\rm SH}^2 g_{\rm eff}^{\uparrow\downarrow}]_{\rm Pt@RT} = 9.8 \times 10^{16}\ {\rm m}^{-2}$. The SMR data presented in Fig. 5 and $\Delta\rho_1/\rho_0$ in Eq. (3), from which we extract the values of $\theta_{\rm SH}^2 g_{\rm eff}^{\uparrow\downarrow}$, are both normalized by R_0 in order to eliminate its contributions since the baseline resistance of the samples is different.

Note that when the effect of noncollinear domains is not taken into account in the model, the fitting can lead to an underestimation by almost two orders of magnitude in $[\theta_{\rm SH}^2\, G_r]$. The difference between the two approaches becomes clearer by fitting the SMR response of the CFO/Pt@HT sample shown in Fig. 5(e). The best fitting taking into account collinear and noncollinear magnetic domains is shown by the solid red line using the parameters $\Delta\rho_1/\rho_0 = 0.035$, $f_{\rm coll} = 0.50$, $\beta_0^{\rm coll} = -0.6^\circ$, and $\beta_0^{\rm noncoll} = -0.6^\circ$ so that we obtain $[\theta_{\rm SH}^2\, G_r]_{\rm Pt@HT} = 3.1 \times 10^{15}\ \Omega^{-1}\ {\rm m}^{-2}$ ($[\theta_{\rm SH}^2 g_{\rm eff}^{\uparrow\downarrow}]_{\rm Pt@HT} = 7.9 \times 10^{18}\ {\rm m}^{-2}$). As we can note, the Pt layer deposited at (400 °C) has a substantial effect on the interfacial spin transport and spin-to-charge (vice versa) current conversion process.

As a final remark, we discuss the γ and α rotation ADMR measurements. For a nearly saturated magnetization, during the γ rotation $m_t \approx 0$, and the SMR effect does not contribute to the measured R_L. Figure 5(a) shows that the angular dependence of $\Delta R_L(\gamma)/R_0$ of the CFO/Pt@RT sample oscillates with a very small amplitude of $\approx 2.4 \times 10^{-5}$. Moreover, in the absence of AMR, Eq. (1) becomes zero, so that the R_L variation is given uniquely by Eq. (2), and it is expected that the $R_L(\alpha)$ and $R_L(\beta)$ amplitudes coincide, as shown in the Figs. 5(b) and 5(c). In contrast, Figs. 5(d) and 5(f) reveal an amplitude of two orders of magnitude larger ($\approx 3 \times 10^{-3}$). From the $R_L(\alpha)$ oscillation, we can observe that the dominant effects are related to the spin-orbit coupling in the Pt and in the (Fe,Co)-Pt alloy, so as to exhibit a combination of AMR and SMR but with mostly AMR contribution. This corroborates with the $R_L(\gamma)$ oscillation that follows a $\sin^2\gamma$ dependence, as expected from the AMR effect in Eq. (1).

To gain a deeper understanding of the underlying physical mechanism behind the SMR in CFO/Pt samples, we provide a schematic illustration of spin structures considering collinear and noncollinear magnetic domains. Figure 6(a) illustrates the SMR process in FMI/NM structures. The amount of spin current at the interface can be modeled in terms of the magnetization direction $\boldsymbol{M}$ relative to $\boldsymbol{\sigma}$. The situation ($\boldsymbol{M} \perp \boldsymbol{\sigma}$; right sketch) corresponds to maximal spin transfer and thus large resistance, while for the ($\boldsymbol{M} \parallel \boldsymbol{\sigma}$; (left sketch) leads to a small resistance. These configurations are well described considering collinear magnetic domains, since the net magnetic moment ($\boldsymbol{M_N}$) follows the applied magnetic field ($\boldsymbol{H}$), as sketched in Fig. 6(b). On the other hand, the use of the same approach for magnetic materials with higher complexity becomes doubtful. Among these, we can mention the CFO, which is largely dependent on the preparation conditions, and has its surface energy changed due to some cationic distribution. The ideal insulating ferrimagnetic CFO is constituted of two sublattices: one tetrahedral [T] composed of Fe^{3+} and the other octahedral [O] with Fe^{3+} and Co^{2+} being the Fe^{3+} ions equality distributed in the [T] and [O] sublattices. The magnetic spins configuration with noncollinear magnetic domain, considering the ideal CFO, is sketched in Fig. 6(c). For this configuration, none of the magnetic moments, $\boldsymbol{M_A}$ (magnetic moment of the [T] sublattice) and $\boldsymbol{M_B}$ (magnetic moment of the [O] sublattice), are parallel to the net magnetic moment ($\boldsymbol{M_N}$), since the antiferromagnetic coupling between magnetic moments at the [T] and [O] sublattices is strong. If we consider, e.g., that the $\boldsymbol{M_B}$ orientation is dominant in spin transfer by interface, a partially large resistance shall appear in a condition corresponding, e.g., to $\boldsymbol{M} \parallel \boldsymbol{\sigma}$ ($\beta = 90^\circ$), giving rise to the fourfold symmetry in the β scan. In addition, the orientation of the net magnetization is determined by the applied magnetic field $\boldsymbol{H}$ that is smaller than the field exchange coupling between the sublattices. Therefore, the SMR results obtained for the CFO/Pt@HT can be explained and

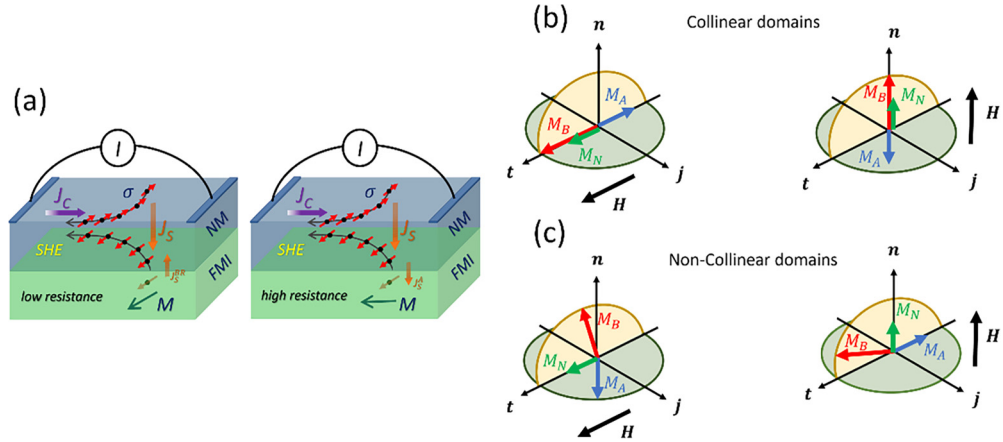

FIG. 6. (a) Schematic illustration of the spin Hall magnetoresistance process in FMI/NM structures. The transverse spin current (J_S) created by the spin Hall effect, can be absorbed ($\boldsymbol{M}\perp\boldsymbol{\sigma}$; right sketch) or reflected ($\boldsymbol{M}\parallel\boldsymbol{\sigma}$; left sketch) at the FMI/NM interface. The back-reflected spin current (J_S^{BR}) is converted into an additional charge current (J_C) due to inverse spin Hall effect. The difference in resistance between both magnetization orientations leads to SMR. Schematic spin configuration considering the (b) collinear and (c) noncollinear domains for the insulating ferrimagnetic CFO.

understood by means of a spin configuration model that takes into account the noncollinear magnetic domains at the interface.

VII. SPIN SEEBECK EFFECT EXPERIMENTS

The large enhancement in the $\theta_{SH}^2 g_{eff}^{\uparrow\downarrow}$ produced by the thermally induced interfacial magnetic modification in CFO/Pt bilayers revealed by the SMR measurements must also be noticed in other phenomena relying on the spin-to-charge conversion process, such as the SSE. It consists in the generation of a spin current by a temperature gradient across a layer of a magnetic insulator that is detected by the voltage created along an attached metallic layer due to its conversion into a charge current [55–62]. The SSE has been widely studied in FMI/NM bilayers [55–62] and also in bilayers made of an antiferromagnetic material in contact with a nonmagnetic metallic film [63–69]. To confirm the SMR results discussed in the last section, we perform SSE experiments with the same two CFO/Pt samples.

The SSE measurements are performed by applying a temperature difference between the side with the Pt strip and the substrate following the steps employed in Ref. [68], but using a modified sample holder as described in the following and illustrated in Fig. 7(a). The heater is replaced by a strain gauge sensor of 350 Ω mounted on a small silver plate. The heater is then attached to the side of the Pt layer through a copper plate. The substrate side is maintained in thermal contact using a second silver plate attached to the copper block. The temperature difference ΔT across the sample is measured using two calibrated Cernox thermometers (model CX-1050-SD-HT). One of the thermometers is attached to the silver plate close to the heater, while the other is attached to the silver plate on the copper block. The strain gauge, the thermometers, and the silver plates are attached by using GE varnish, which is well known for having good thermal properties and for being widely used in applications at low temperatures. The sample holder is mounted on a dc resistivity puck of a PPMS and Au leads are used to attach the thermometers, the heater, and the Pt film to the puck. The electrical contacts are made with silver paint. An external dc power supply is used for setting the temperature difference ΔT across the sample. The PPMS operates in the user bridge mode with the temperature stabilized to within $\Delta T = 0.01$ K and varies from 5 to 300 K. The measurements are performed under high vacuum using a cryogenic pump coupled to the PPMS. The magnetic field H applied in the plane of the sample and transversely to the long dimension of the Pt strip is swept from −85 kOe to +85 kOe with varying steps: 5 kOe for 85 kOe > $|H_0|$ > 5 kOe and 1 kOe for $|H_0| < 5$ kOe. The voltage produced in the Pt film by the SSE-ISHE effects is then measured directly by the PPMS with several temperature differences, $\Delta T = T - T_{Base}$. Before recording the ΔT data, the temperature is monitored as a function of time until the thermal stabilization is achieved.

Figure 7(b) shows the room-temperature magnetic field dependence of the SSE current (I_{SSE}) in the Pt layer of the CFO/Pt@HT sample, obtained by dividing the measured voltage by the Pt layer resistance $I_{SSE} = V_{SSE}/R_{Pt}$, for several values of the temperature difference ΔT. Notice that we use the SSE current, and not the voltage, to eliminate the influence of the Pt layer resistance. The copper block temperature (T_{Base}) is maintained at 300 K, so that the Pt layer is at a temperature $T = T_{base} + \Delta T$. Figure 7(c) shows the SSE current versus applied magnetic field measured at 300 K for the CFO/Pt@RT and CFO/Pt@HT samples for a temperature difference $\Delta T = 9.7$ K. Figure 7(d) shows the SSE current measured at $H = 50$ kOe as a function of the temperature difference. The difference in slope values in the $I_{SSE} \times \Delta T$ curves for the CFO/Pt@RT and CFO/Pt@HT samples reveals a pivotal change in the spin transport through the CFO-Pt interface produced by the heat treatment.

The data in Fig. 7 are completely consistent with the picture of the spin Seebeck effect. As shown in Refs. [58,70], the measured voltage is due to the charge current in the Pt

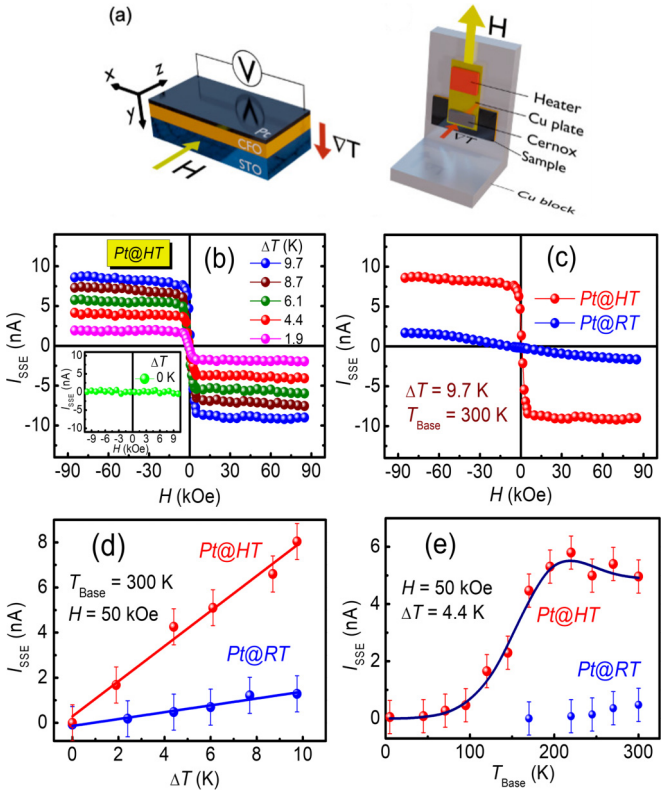

FIG. 7. (a) Schematic illustration of the experimental setup used to measure the voltages generated by spin Seebeck effect in the STO/CFO/Pt heterostructures and a sketch of the sample holder mount displaying the heater and thermometer. (b) Variation with magnetic field H of the SSE current in the Pt layer of the CFO/Pt@HT sample for six values of the temperature difference ΔT, with the copper block at $T_{\rm Base} = 300\,$K. The data for $\Delta T = 0$ is shown in the inset. (c) SSE current *versus* field H measured in the CFO/Pt@HT and CFO/Pt@HT samples with a temperature difference $\Delta T = 9.7$ K and $T_{\rm Base} = 300\,$K. (d) Variation with temperature difference ΔT of the SSE current measured with $H = 50\,$kOe and $T_{\rm Base} = 300\,$K. (e) Temperature dependence of the SSE current measured in the CFO/Pt@HT and CFO/Pt@RT samples with $H = 50\,$kOe and $\Delta T = 4.4$ K. The solid blue line for the CFO/Pt@HT data is a guide for the eyes.

layer produced by the ISHE conversion of the spin current generated by the temperature difference applied to the CFO/Pt bilayer. The application of a temperature gradient ∇T across the CFO layer generates a spin current carried by magnons with density given by $J_S = -C_S g_{\rm eff}^{\uparrow\downarrow} \nabla T$, where C_S is a coefficient that depends on the FMI parameters, such as saturation magnetization ($C_S \propto 1/M_{\rm CFO}$), magnon diffusion coefficient, temperature, and applied magnetic field intensity [69]. The spin current flows across the CFO/Pt interface into the Pt layer and is converted into a charge current by the ISHE with density given by $\vec{J}_c = \theta_{SH} \vec{J}_s \times \hat{\sigma}$, where $\theta_{\rm SH}$ is the spin Hall angle and $\hat{\sigma}$ is the spin polarization. As the field is scanned and reversed at $H = 0$, the sign of $\hat{\sigma}$ in the spin current changes, and so does the voltage signal. Figure 7(d) shows that the SSE current in the two samples varies linearly with the temperature difference, as expected from Eq. (8) for the SSE. A comparison of the slopes of the two linear fits shows that the SSE in the CFO/Pt@HT sample is larger than that in the CFO/Pt@RT sample by a factor of 5.1. The variation of the SSE current with the base temperature measured at $H = 50\,$kOe with $\Delta T = 4.4\,$K for the CFO/Pt@HT and CFO/Pt@RT samples is shown in Fig. 7(e). The $I_{\rm SSE}$ vs $T_{\rm Base}$ for the CFO/Pt@RT sample is very small at room temperature and undetectable at low temperatures. Nevertheless, for both samples, the temperature variation of the SSE has a shape that is similar to the one measured in YIG, which is explained quantitatively by the magnonic spin current model [58,70].

VIII. DISCUSSION AND CONCLUSIONS

We use angle-dependent magnetoresistance and spin Seebeck effect to investigate the spin-to-charge current interconversion process in CFO/Pt bilayers, with the Pt deposited at room temperature (CFO/Pt@RT) and at high temperature (CFO/Pt@HT). Here, we discuss the results of the spin-to-charge interconversion process obtained from both techniques that are entirely in agreement. To obtain further information on the spin transport through the CFO-Pt interface, we compare both parameters $\theta_{\rm SH}^2$ and $g_{\rm eff}^{\uparrow\downarrow}$ for such samples by means of SMR data [Figs. 5(b)–5(e)] and the slopes obtained from the $I_{\rm SSE}$ vs ΔT curves measured by SSE in Fig. 7(d).

From SMR, we obtain $[\theta_{\rm SH}^2 g_{\rm eff}^{\uparrow\downarrow}]_{\rm Pt@RT}^{(SMR)} = 2.7 \times 10^{18}\ {\rm m}^{-2}$ and $[\theta_{\rm SH}^2 g_{\rm eff}^{\uparrow\downarrow}]_{\rm Pt@HT}^{(SMR)} = 7.9 \times 10^{18}\ {\rm m}^{-2}$. Now, to confirm these results, we determine both parameters from the SSE measurements. From the magnonic spin current model for SSE, the relation between the $I_{\rm SSE}$ current and the temperature gradient ∇T is given by

$$I_{\rm SSE}/\nabla T = \theta_{\rm SH} g_{\rm eff}^{\uparrow\downarrow} w \lambda_{\rm NM} \frac{2e}{\hbar} \tanh\left(\frac{t_{\rm NM}}{2\lambda_{\rm NM}}\right) C_S \rho_{FM} \cos\varphi, \tag{8}$$

where ρ_{FM} is a factor representing the finite-size effect of the FM layer thickness, R_N and w are the resistance and width of the Pt layer, respectively, and φ is the angle of the spin polarization determined by the direction of the applied magnetic field. Although we are not able to reach reliable values for the coefficient C_S for our magnetic structures, we know that $C_S \propto 1/M_{\rm CFO}$ [58,70]. Then, we take the ratio between the SSE slope values in Fig. 7(d), so that $M_{\rm CFO@RT}[\theta_{\rm SH} g_{\rm eff}^{\uparrow\downarrow}]_{\rm Pt@HT}^{(SSE)} / M_{\rm CFO@HT}[\theta_{\rm SH} g_{\rm eff}^{\uparrow\downarrow}]_{\rm Pt@RT}^{(SSE)} = 5.1$. Then, considering the magnetization at high fields taken from the magnetization curves acquired for our structures, $M_{\rm CFO@HT} = 350$ emu/cm^3 and $M_{\rm CFO@RT} = 241$ emu/cm^3, we achieve $[\theta_{\rm SH} g_{\rm eff}^{\uparrow\downarrow}]_{\rm Pt@HT}^{(SSE)} / [\theta_{\rm SH} g_{\rm eff}^{\uparrow\downarrow}]_{\rm Pt@RT}^{(SSE)} = 7.4$. Using the same approach for the SMR measurements, we find $[\theta_{\rm SH}^2 g_{\rm eff}^{\uparrow\downarrow}]_{\rm Pt@HT}^{(SMR)} / [\theta_{\rm SH}^2 g_{\rm eff}^{\uparrow\downarrow}]_{\rm Pt@RT}^{(SMR)} = 2.9$. From the two ratios, finally we obtain $\theta_{\rm SH}^{\rm (Pt@HT)} = 0.39 \times \theta_{\rm SH}^{\rm (Pt@RT)}$ and $g_{\rm eff}^{\uparrow\downarrow({\rm Pt@HT})} = 19 \times g_{\rm eff}^{\uparrow\downarrow({\rm Pt@RT})}$.

The significant increase in the spin-mixing conductance ($g_{\rm eff}^{\uparrow\downarrow}$) for the CFO/Pt@HT sample is primarily related to the enhancement of the magnetic moment arisen at the interface due to the formation of the ferromagnetic (Fe,Co)-Pt alloy, which is a consequence of the structural, electronic, and

magnetic reconstructions at the interface between Pt and the insulating ferrimagnetic CFO due to heat treatment. As has been predicted, the enhancement of the spin torque efficiency depends on the density of magnetic ions at the FMI surface, such that the insertion of magnetic atomic layers increases the spin-mixing conductance [71]. In accordance with that, an improvement of the spin transmission has been observed by inserting an ultrathin ferromagnetic layer between the insulating ferrimagnetic oxide and the Pt layer, which is due to the increase of the spin-mixing conductance by increasing the magnetic density at the interface [72–75]. On the other hand, the decrease in $\theta_{SH}^{(HT)}$ for the CFO/Pt@HT sample is also associated with the (Co, Fe)-Pt alloy layer. Knowing the spin Hall angle, defined by $\theta_{SH} = \sigma_{SH}/\sigma$, where σ_{SH} is the transverse spin conductivity, we expect that an increase in the conductivity σ due to the (Co, Fe)-Pt alloy implies a decrease in θ_{SH}.

In summary, we report on the spin-to-charge interconversion process in CFO/Pt bilayers grown onto STO(001) substrates, so that the CFO thin films are (001) fully textured. As spin transmission and spin backflow are driven by interface phenomena, here we show quite a difference between the ADMR and the SSE results when the Pt layer is deposited under two different temperatures. While for the sample wherein the Pt layer is grown at room temperature the results are in accordance with those reported for interfaces with more magnetic and electronic stability, for a sample where the Pt layer is grown at high temperature, the results are strikingly different. The high-temperature deposition of the Pt layer may have potentiated and induced a new interfacial magnetic phase like (Fe,Co)-Pt alloy, generating an increase in the SSE signal besides an additional contribution to ADMR so that noncollinear and collinear magnetic domains should coexist at the interface. Therefore, our results show that SMR is a highly sensitive probe to surface magnetism that can be used to identify even complex magnetic configurations, including collinear and noncollinear magnetic domains in highly resistive ferrimagnetic oxides in contact with normal metals. Furthermore, we also observe a strong dependence of the SSE current with the Pt layer deposition temperature which is consistent with SMR. From them, we obtain for the CFO/Pt@HT sample an interfacial spin-mixing conductance more than one order of magnitude larger than for the CFO/Pt@RT sample. We interpret the increase of $g_{eff}^{\uparrow\downarrow}$ in terms of unexpected magnetic reconstructions, which lead to an enhancement in the magnetic moment arisen at the interface. Thus, since the spin-mixing conductance defines the efficiency of spin current transmission through the interface, the spinel ferrite cobalt in contact with normal metal with suitable heat treatment is a promising material for spintronics device applications.

ACKNOWLEDGMENTS

This research was supported in Brazil by Conselho Nacional de Desenvolvimento Científico e Tecnológico (CNPq), Coordenação de Aperfeiçoamento de Pessoal de Nível Superior (CAPES), Financiadora de Estudos e Projetos (FINEP), Fundação de Amparo à Promoção da Ciência, Tecnologia e Inovação do Estado do Rio Grande do Norte (FAPERN), Fundação de Amparo à Ciência e Tecnologia do Estado de Pernambuco (FACEPE), and Fundação de Amparo à Pesquisa do Estado de São Paulo (FAPESP) Grant No. 2022/04496-0; and in Chile by Fondo Nacional de Desarrollo Científico y Tecnológico (FONDECYT) Grant No. 1210641 and FONDEQUIP EQM180103. Ministerio de Ciencia, Universidades e Investigación (SPAIN) (Grants No. PID2020-118479RB-I00/AEI/10.13039/501100011033 and No. TED2021-129857B-I00. The authors acknowledge support of the INCT of Spintronics and Advanced Magnetic Nanostructures (INCT-SpinNanoMag), CNPq 406836/2022–1.

[1] *Spin Current*, 2nd ed., edited by S. Maekawa, S. O. Valenzuela, E. Saitoh, and T. Kimura (Oxford University Press, New York, 2017).

[2] S. Y. Huang, X. Fan, D. Qu, Y. P. Chen, W. G. Wang, J. Wu, T. Y. Chen, J. Q. Xiao, and C. L. Chien, Transport magnetic proximity effects in platinum, Phys. Rev. Lett. **109**, 107204 (2012).

[3] Y. M. Lu, Y. Choi, C. M. Ortega, X. M. Cheng, J. W. Cai, S. Y. Huang, L. Sun, and C. L. Chien, Pt magnetic polarization on $Y_3Fe_5O_{12}$ and magnetotransport characteristics, Phys. Rev. Lett. **110**, 147207 (2013).

[4] B. F. Miao, S. Y. Huang, D. Qu, and C. L. Chien, Physical origins of the new magnetoresistance in Pt/YIG, Phys. Rev. Lett. **112**, 236601 (2014).

[5] S. O. Valenzuela and M. Tinkham, Direct electronic measurement of the spin Hall effect, Nature (London) **442**, 176 (2006).

[6] A. Hoffmann, Spin Hall effects in metals, IEEE Trans. Magn. **49**, 5172 (2013).

[7] V. M. Edelstein, Spin polarization of conduction electrons induced by electric current in two-dimensional asymmetric electron systems, Solid State Commun. **73**, 233 (1990).

[8] A. Manchon, H. C. Koo, J. Nitta, S. M. Frolov, and R. A. Duine, New perspectives for Rashba spin-orbit coupling, Nat. Mater. **14**, 871 (2015).

[9] A. Soumyanarayanan, N. Reyren, A. Fert, and C. Panagopoulos, Emergent phenomena induced by spin-orbit coupling at surfaces and interfaces, Nature (London) **539**, 509 (2016).

[10] Y. Ando and M. Shiraishi, Spin to charge interconversion phenomena in the interface and surface states, J. Phys. Soc. Jpn. **86**, 011001 (2017).

[11] W. Han, Y. Otani, and S. Maekawa, Quantum materials for spin and charge conversion, npj Quantum Mater. **3**, 27 (2018).

[12] J. C. Rojas Sánchez, L. Vila, G. Desfonds, S. Gambarelli, J. P. Attané, J. M. De Teresa, C. Magén, and A. Fert, Spin-to-charge conversion using Rashba coupling at the interface between nonmagnetic materials, Nat. Commun. **4**, 2944 (2013).

[13] J. E. Hirsch, Spin Hall effect, Phys. Rev. Lett. **83**, 1834 (1999).

[14] A. Azevedo, L. H. V. Leão, R. L. Rodriguez-Suarez, A. B. Oliveira, and S. M. Rezende, dc effect in ferromagnetic resonance: Evidence of the spin-pumping effect?, J. Appl. Phys. **97**, 10C715 (2005).

[15] E. Saitoh, M. Ueda, H. Miyajima, and G. Tatara, Conversion of spin current into charge current at room temperature: Inverse spin-Hall effect, Appl. Phys. Lett. **88**, 182509 (2006).

[16] S. Maekawa, H. A. Adachi, K. Uchida, J. Ieda, and E. Saitoh, Spin current: Experimental and theoretical aspects, J. Phys. Soc. Jpn. **82**, 102002 (2013).

[17] J. Sinova, S. O. Valenzuela, J. Wunderlich, C. H. Back, and T. Jungwirth, Spin Hall effects, Rev. Mod. Phys. **87**, 1213 (2015).

[18] H. Nakayama, M. Althammer, Y.-T. Chen, K. Uchida, Y. Kajiwara, D. Kikuchi, T. Ohtani, S. Geprägs, M. Opel, S. Takahashi, R. Gross, G. E. W. Bauer, S. T. B. Goennenwein, and E. Saitoh, Spin Hall magnetoresistance induced by a nonequilibrium proximity effect, Phys. Rev. Lett. **110**, 206601 (2013).

[19] C. Hahn, G. de Loubens, O. Klein, M. Viret, V. V. Naletov, and J. Ben Youssef, Comparative measurements of inverse spin Hall effects and magnetoresistance in YIG/Pt and YIG/Ta, Phys. Rev. B **87**, 174417 (2013).

[20] M. Weiler, M. Althammer, M. Schreier, J. Lotze, M. Pernpeintner, S. Meyer, H. Huebl, R. Gross, A. Kamra, J. Xiao, Y.-T. Chen, H. Jiao, G. E. W. Bauer, and S. T. B. Goennenwein, Experimental test of the spin mixing interface conductivity concept, Phys. Rev. Lett. **111**, 176601 (2013).

[21] M. Althammer, S. Meyer, H. Nakayama, M. Schreier, S. Altmannshofer, M. Weiler, H. Huebl, S. Geprägs, M. Opel, R. Gross *et al.*, Quantitative study of the spin Hall magnetoresistance in ferromagnetic insulator/normal metal hybrids, Phys. Rev. B **87**, 224401 (2013).

[22] Y. Hui, W. Cheng, Z. Zhang, H. Wang, C. Xie, and X. Miao, Transport mechanism of the magnetoresistance effects in Ta/$CoFe_2O_4$ nanostructures, Appl. Phys. Lett. **110**, 192404 (2017).

[23] J. Q. Guo, K. K. Meng, T. Z. Zhang, J. J. Liu, J. K. Chen, Y. Wu, X. G. Xu, and Y. Jiang, Spin Hall magnetoresistance of $CoFe_2O_4$/Pt heterostructures with interface non-collinear magnetic configurations, Appl. Phys. Lett. **121**, 142403 (2022).

[24] D. Chen, Y. Xu, S. Tong, W. Zheng, Y. Sun, J. Lu, N. Lei, D. Wei, and J. Zhao, Noncollinear spin state and unusual magnetoresistance in ferrimagnet Co-Gd, Phys. Rev. Mater. **6**, 014402 (2022).

[25] B.-W. Dong, J. Cramer, K. Ganzhorn, H. Y. Yuan, E.-J. Guo, S. T. B. Goennenwein, and M. Kläui, Spin Hall magnetoresistance in the non-collinear ferrimagnet GdIG close to the compensation temperature, J. Phys.: Condens. Matter **30**, 035802 (2018).

[26] K. Ganzhorn, J. Barker, R. Schlitz, B. A. Piot, K. Ollefs, F. Guillou, F. Wilhelm, A. Rogalev, M. Opel, M. Althammer, S. Geprägs, H. Huebl, R. Gross, G. E. W. Bauer, and S. T. B. Goennenwein, Spin Hall magnetoresistance in a canted ferrimagnet, Phys. Rev. B **94**, 094401 (2016).

[27] M. Isasa, A. Bedoya-Pinto, S. Vélez, F. Golmar, F. Sánchez, Luis. E. Hueso, J. Fontcuberta, and F. Casanova, Spin Hall magnetoresistance at Pt/$CoFe_2O_4$ interfaces and texture effects, Appl. Phys. Lett. **105**, 142402 (2014).

[28] M. Valvidares, N. Dix, M. Isasa, K. Ollefs, F. Wilhelm, A. Rogalev, F. Sánchez, E. Pellegrin, A. Bedoya-Pinto, P. Gargiani, L. E. Hueso, F. Casanova, and J. Fontcuberta, Absence of magnetic proximity effects in magnetoresistive Pt/$CoFe_2O_4$ hybrid interfaces, Phys. Rev. B **93**, 214415 (2016).

[29] M. Isasa, S. Vélez, E. Sagasta, A. Bedoya-Pinto, N. Dix, F. Sánchez, L. E. Hueso, J. Fontcuberta, and F. Casanova, Spin Hall magnetoresistance as a probe for surface magnetization in Pt/$CoFe_2O_4$ bilayers, Phys. Rev. Appl. **6**, 034007 (2016).

[30] H. B. Vasili, M. Gamino, J. Gàzquez, F. Sánchez, M. Valvidares, P. Gargiani, E. Pellegrin, and J. Fontcuberta, Magnetoresistance in hybrid Pt/ $CoFe_2O_4$ bilayers controlled by competing spin accumulation and interfacial chemical reconstruction, ACS Appl. Mater. Interfaces **10**, 12031 (2018).

[31] W. Amamou, I. V. Pinchuk, A. H. Trout, R. E. A. Williams, N. Antolin, A. Goad, D. J. O'Hara, A. S. Ahmed, W. Windl, D. W. McComb, and R. K. Kawakami, Magnetic proximity effect in Pt/$CoFe_2O_4$ bilayers, Phys. Rev. Mater. **2**, 011401(R) (2018).

[32] E.-J. Guo, A. Herklotz, A. Kehlberger, J. Cramer, G. Jakob, and M. Kläui, Thermal generation of spin current in epitaxial $CoFe_2O_4$ thin films, Appl. Phys. Lett. **108**, 022403 (2016).

[33] F. Rigato, J. Geshev, V. Skumryev, and J. Fontcuberta, The magnetization of epitaxial nanometric $CoFe_2O_4$ (001) layers, J. Appl. Phys. **106**, 113924 (2009).

[34] S. Matzen, J.-B. Moussy, R. Mattana, F. Petroff, C. Gatel, B. Warot-Fonrose, J. C. Cezar, A. Barbier, M.-A. Arrio, and P. Sainctavit, Restoration of bulk magnetic properties by strain engineering in epitaxial $CoFe_2O_4$ (001) ultrathin films, Appl. Phys. Lett. **99**, 052514 (2011).

[35] F. Eskandari, S. B. Porter, M. Venkatesan, P. Kameli, K. Rode, and J. M. D. Coey, Magnetization and anisotropy of cobalt ferrite thin films, Phys. Rev. Mater. **1**, 074413 (2017).

[36] D. T. Margulies, F. T. Parker, M. L. Rudee, F. E. Spada, J. N. Chapman, P. R. Aitchison, and A. E. Berkowitz, Origin of the anomalous magnetic behavior in single crystal Fe_3O_4 films, Phys. Rev. Lett. **79**, 5162 (1997).

[37] F. C. Voogt, T. T. M. Palstra, L. Niesen, O. C. Rogojanu, M. A. James, and T. Hibma, Superparamagnetic behavior of structural domains in epitaxial ultrathin magnetite films, Phys. Rev. B **57**, R8107 (1998).

[38] W. Eerenstein, T. T. M. Palstra, S. S. Saxena, and T. Hibma, Spin-polarized transport across sharp antiferromagnetic boundaries, Phys. Rev. Lett. **88**, 247204 (2002).

[39] J.-B. Moussy, S. Gota, A. Bataille, M.-J. Guittet, M. Gautier-Soyer, F. Delille, B. Dieny, F. Ott, and T. D. Doan, P. Warin, P. Bayle-Guillemaud, C. Gatel, and E. Snoeck, Thickness dependence of anomalous magnetic behavior in epitaxial Fe_3O_4(111) thin films: Effect of density of antiphase boundaries, Phys. Rev. B **70**, 174448 (2004).

[40] B. C. Meyer, T. C. R. Rocha, S. A. L. Luiz, A. C. Pinto, and H. Westfahl, Jr., Simulation and optimization of the SIRIUS IPE soft x-ray beamline, *Proceedings of SPIE, Advances in Computational Methods for X-Ray Optics IV* (SPIE, 2017), Vol. 10388.

[41] J. de la Figuera, A. Quesada, L. Martín-García, M. Sanz, M. Oujja, M. Castillejo, A. Mascaraque, A. T. N'Diaye, M. Foerster, L. Aballe, and J. F. Marco, Mössbauer and magnetic properties of coherently mixed magnetite-cobalt ferrite grown by infrared pulsed-laser deposition, Croat. Chem. Acta **88**, 453 (2015).

[42] J. A. Moyer, C. A. F. Vaz, E. Negusse, D. A. Arena, and V. E. Henrich, Controlling the electronic structure of $Co_{1-x}Fe_{2+x}O_4$ thin films through iron doping, Phys. Rev. B **83**, 035121 (2011).

[43] I. C. Nlebedim, N. Ranvah, P. I. Williams, Y. Melikhov, J. E. Snyder, A. J. Moses, and D. C. Jiles, Effect of heat treatment on

the magnetic and magnetoelastic properties of cobalt ferrite, J. Magn. Magn. Mater. **322**, 1929 (2010).
[44] M. Ziese and H. J. Blythe, Magnetoresistance in magnetite, J. Phys.: Condens. Matter **12**, 13 (2000).
[45] Z. Ding, B. L. Chen, J. H. Liang, J. Zhu, J. X. Li, and Y. Z. Wu, Spin Hall magnetoresistance in Pt/Fe_3O_4 thin films at room temperature, Phys. Rev. B **90**, 134424 (2014).
[46] J. M. D. Coey, A. E. Berkowitz, L. I. Balcells, F. F. Putris, and F. T. Parker, Magnetoresistance of magnetite, Appl. Phys. Lett. **72**, 734 (1998).
[47] Y.-T. Chen, S. Takahashi, H. Nakayama, M. Althammer, S. T. B. Goennenwein, E. Saitoh, and G. E. W. Bauer, Theory of spin Hall magnetoresistance, Phys. Rev. B **87**, 144411 (2013).
[48] W. Lin and C. L. Chien, Electrical detection of spin backflow from an antiferromagnetic insulator/$Y_3Fe_5O_{12}$ interface, Phys. Rev. Lett. **118**, 067202 (2017).
[49] D. Hou, Z. Qiu, J. Barker, K. Sato, K. Yamamoto, S. Vélez, J. M. Gomez-Perez, L. E. Hueso, F. Casanova, and E. Saitoh, Tunable sign change of spin Hall magnetoresistance in Pt/NiO/YIG structures, Phys. Rev. Lett. **118**, 147202 (2017).
[50] R. C. Bhatt, L.-X. Ye, N. T. Hai, J.-C. Wu, and T.-h. Wu, Spin-flop led peculiar behavior of temperature-dependent anomalous Hall effect in Hf/Gd-Fe-Co, J. Mag. Magn. Mater. **537**, 168196 (2021).
[51] G. R. Hoogeboom, A. Aqeel, T. Kuschel, T. T. M. Palstra, and B. J. van Wees, Negative spin Hall magnetoresistance of Pt on the bulk easy-plane antiferromagnet NiO, Appl. Phys. Lett. **111**, 052409 (2017).
[52] J. Fischer, O. Gomonay, R. Schlitz, K. Ganzhorn, N. Vlietstra, M. Althammer, H. Huebl, M. Opel, R. Gross, S. T. B. Goennenwein, and S. Geprägs, Spin Hall magnetoresistance in antiferromagnet/heavy-metal heterostructures, Phys. Rev. B **97**, 014417 (2018).
[53] L. Baldrati, A. Ross, T. Niizeki, C. Schneider, R. Ramos, J. Cramer, O. Gomonay, M. Filianina, T. Savchenko, D. Heinze, A. Kleibert, E. Saitoh, J. Sinova, and M. Kläui, Full angular dependence of the spin Hall and ordinary magnetoresistance in epitaxial antiferromagnetic NiO(001)/Pt thin films, Phys. Rev. B **98**, 024422 (2018).
[54] M. Gamino, D. S. Maior, L. H. Vilela-Leão, R. L. Rodríguez-Suárez, F. L. A. Machado, A. Azevedo, and S. M. Rezende, Physical origins of the magnetoresistance of platinum in contact with polycrystalline antiferromagnetic NiO, J. Magn. Magn. Mater. **475**, 586 (2019).
[55] K. Uchida, H. Adachi, T. Ota, H. Nakayama, S. Maekawa, and E. Saitoh, Observation of longitudinal spin-Seebeck effect in magnetic insulators, Appl. Phys. Lett. **97**, 172505 (2010).
[56] G. E. W. Bauer, E. Saitoh, and B. J. van Wees, Spin caloritonics, Nat. Mater. **11**, 391 (2012).
[57] S. R. Boona, R. C. Myers, and J. P. Heremans, Spin caloritonics, Energy Environ. Sci. **7**, 885 (2014).
[58] S. M. Rezende, R. L. Rodríguez-Suárez, R. O. Cunha, A. R. Rodrigues, F. L. A. Machado, G. A. Fonseca Guerra, J. C. López Ortiz, and A. Azevedo, Magnon spin-current theory for the longitudinal spin-Seebeck effect, Phys. Rev. B **89**, 014416 (2014).
[59] K. Uchida, M. Ishida, T. Kikkawa, A. Kirihara, T. Murakami, and E. Saitoh, Longitudinal spin Seebeck effect: From fundamentals to applications, J. Phys.: Condens. Matter **26**, 343202 (2014).
[60] H. Yu, S. D. Brechet, and J.-P. Ansermet, Spin caloritronics, origin and outlook, Phys. Lett. A **381**, 825 (2017).
[61] K.-I. Uchida, Spin caloritronics, *Materials Science and Materials Engineering* (Elsevier, Amsterdam, 2022).
[62] S. Maekawa, T. Kikkawa, H. Chudo, J.-I. Ieda, and E. Saitoh, Spin and spin current—From fundamentals to recent progress, J. Appl. Phys. **133**, 020902 (2023).
[63] S. Seki, T. Ideue, M. Kubota, Y. Kozuka, R. Takagi, M. Nakamura, Y. Kaneko, M. Kawasaki, and Y. Tokura, Thermal generation of spin current in an antiferromagnet, Phys. Rev. Lett. **115**, 266601 (2015).
[64] S. M. Wu, W. Zhang, A. KC, P. Borisov, J. E. Pearson, J. S. Jiang, D. Lederman, A. Hoffmann, and A. Bhattacharya, Antiferromagnetic spin Seebeck effect, Phys. Rev. Lett. **116**, 097204 (2016).
[65] J. Holanda, D. S. Maior, O. Alves Santos, L. H. Vilela-Leão, J. B. S. Mendes, A. Azevedo, R. L. Rodríguez-Suárez, and S. M. Rezende, Spin Seebeck effect in the antiferromagnet nickel oxide at room temperature, Appl. Phys. Lett. **111**, 172405 (2017).
[66] Y. Shiomi, R. Takashima, D. Okuyama, G. Gitgeatpong, P. Piyawongwatthana, K. Matan, T. J. Sato, and E. Saitoh, Spin Seebeck effect in the polar antiferromagnet α-$Cu_2V_2O_7$, Phys. Rev. B **96**, 180414(R) (2017).
[67] J. Li, Z. Shi, V. H. Ortiz, M. Aldosary, C. Chen, V. Aji, P. Wei, and J. Shi, Spin Seebeck effect from antiferromagnetic magnons and critical spin fluctuations in epitaxial FeF_2 films, Phys. Rev. Lett. **122**, 217204 (2019).
[68] P. R. T. Ribeiro, F. L. A. Machado, M. Gamino, A. Azevedo, and S. M. Rezende, Spin Seebeck effect in antiferromagnet nickel oxide in wide ranges of temperature and magnetic field, Phys. Rev. B **99**, 094432 (2019).
[69] W. Yuan, J. Li, and J. Shi, Spin current generation and detection in uniaxial antiferromagnetic insulators, Appl. Phys. Lett. **117**, 100501 (2020).
[70] S. M. Rezende, R. L. Rodríguez-Suárez, and A. Azevedo, Magnon diffusion theory for the spin Seebeck effect in ferromagnetic and antiferromagnetic insulators, J. Phys. D: Appl. Phys. **51**, 174004 (2018).
[71] X. Jia, K. Liu, K. Xia, and G. E. W. Bauer, Spin transfer torque on magnetic insulators, Europhys. Lett. **96**, 17005 (2011).
[72] D. Kikuchi, M. Ishida, K. Uchida, Z. Qiu, T. Murakami, and E. Saitoh, Enhancement of spin-Seebeck effect by inserting ultra-thin $Fe_{70}Cu_{30}$ interlayer, Appl. Phys. Lett. **106**, 082401 (2015).
[73] H. Yuasa, K. Tamae, and N. Onizuka, Spin mixing conductance enhancement by increasing magnetic density, AIP Adv. **7**, 055928 (2017).
[74] S. Emori, A. Matyushov, H.-M. Jeon, C. J. Babroski, T. Nan, A. M. Belkessam, J. G. Jones, M. E. McConney, G. J. Brown, B. M. Howe, and N. X. Sun, Spin-orbit torque and spin pumping in YIG/Pt with interfacial insertion layers, Appl. Phys. Lett. **112**, 182406 (2018).
[75] H. Shi, Y. Su, Y. Meng, L. Wang, X. Cao, and H. Zhao, Enhanced spin transmission due to interfacial NiFe insertion in YIG/Pt films, Appl. Phys. Lett. **119**, 222404 (2021).